Human Molecular Genetics, 2012, Vol. 21, No. 4 ***799–810***
doi:10.1093/hmg/ddr511
Advance Access published on November 7, 2011

Postnatal neurogenesis generates heterotopias, olfactory micronodules and cortical infiltration following single-cell *Tsc1* deletion

David M. Feliciano[1,2], Jennifer L. Quon[1,2], Tiffany Su[1,2], M. Morgan Taylor[1,2], and Angélique Bordey[12,*]

[1]Department of Neurosurgery and [2]Department of Cellular and Molecular Physiology, Yale University School of Medicine, New Haven, CT, USA

Received September 14, 2011; Revised and Accepted October 31, 2011

Neurological symptoms in tuberous sclerosis complex (TSC) and associated brain lesions are thought to arise from abnormal embryonic neurogenesis due to inherited mutations in *Tsc1* or *Tsc2*. Neurogenesis persists postnatally in the human subventricular zone (SVZ) where slow-growing tumors containing *Tsc*-mutant cells are generated in TSC patients. However, whether *Tsc*-mutant neurons from the postnatal SVZ contribute to brain lesions and abnormal circuit remodeling in forebrain structures remain unexplored. Here, we report the formation of olfactory lesions following conditional genetic *Tsc1* deletion in the postnatal SVZ using transgenic mice or targeted single-cell electroporation. These lesions include migratory heterotopias and olfactory micronodules containing neurons with a hypertrophic dendritic tree. Most significantly, our data identify migrating glial and neuronal precursors that are re-routed and infiltrate forebrain structures (e.g. cortex) and become glia and neurons. These data show that *Tsc1*-mutant cells from the neonatal and juvenile SVZ generate brain lesions and structural abnormalities, which would not be visible using conventional non-invasive imaging. These findings also raise the hypothesis that micronodules and the persistent infiltration of cells to forebrain structures may contribute to network malfunction leading to progressive neuropsychiatric symptoms in TSC.

INTRODUCTION

Tuberous sclerosis complex (TSC) is an autosomal dominant disorder that is associated with lesions in many different organs including in the kidney, skin, heart and brain. The incidence of TSC is estimated between 1:6000 and 1:10 000 individuals (1). TSC is caused by inactivating mutations in one of two tumor suppressor genes, *TSC1* and *TSC2*, which encode hamartin and tuberin, respectively, and lead to hyperactivity of the mammalian target of rapamycin (mTOR) (2). Although TSC affects many organ systems, the neurological symptoms (e.g. seizures, autism, psychiatric problems) cause the most significant disability and morbidity (3–6).

Neurological symptoms in TSC result from anomalies in brain development, in particular cortical neurogenesis, leading to an abnormal circuitry and the formation of brain lesions (7–16). These lesions are thought to occur *in utero* when cortical neurons are generated and migrate to their final location (8). Indeed, cortical lesions have been detected as early as 19 weeks of gestation in humans (17) and were generated following *Tsc1* deletion in embryonic neural progenitor cells and developing neurons (9). Neurogenesis, however, does not stop at birth, but persists in selective regions of the neonatal and adult brain in all species examined, including humans (18–21). This continual generation of new neurons confers plasticity at the cellular and circuit levels. It also raises the possibility that postnatal neurogenesis in individuals with TSC could contribute to specific brain lesions and abnormal circuit remodeling (7,22).

The subventricular zone (SVZ) along the lateral ventricle and the hippocampal subgranular zone of the dentate gyrus are sites of active neurogenesis throughout life (21,23). The SVZ contains the largest pool of neural progenitor cells in

*To whom correspondence should be addressed at: Yale Univ. Sch. Med., 333 Cedar St, FMB 422. New Haven, CT 06520-8082, USA. Tel: +1 2037372515; Fax: +1 2037372159; Email: angelique.bordey@yale.edu

the adult human brain and span the entire cerebrum (19,24–26). During the neonatal period, the SVZ generates both neurons and glia, and essentially neurons in adults (27). Newborn neuroblasts migrate to the olfactory bulb where they differentiate into interneurons (19,20,28). A subset of these neurons also migrates to cortical and subcortical structures most prominently during the neonatal period (29–31). Individuals with TSC display lesions (referred to as nodules or hamartomas) in the forebrain, such as the olfactory and basal ganglia structures (32–38). In addition, they display SVZ nodules and giant cell subependymal astrocytomas (SEGAs) that have been recently generated in mice by deleting *Tsc1* in neonatal neural progenitor cells (39–41). Collectively, these pieces of evidence suggest that *Tsc1*^{null} neurons are continuously generated from the postnatal SVZ, but their contribution to olfactory lesions and alterations in surrounding neuronal circuits remain unexplored.

Using genetic tools including conditional transgenic mice and single-cell genetic targeting, we report that olfactory lesions (i.e. heterotopic and micronodules) are generated from the postnatal SVZ. In addition, we found a continual infiltration of cells, including neurons and glia, from the migratory stream to cortical and subcortical areas. This finding raises new questions regarding the contribution of micronodules and ectopic migration to progressive circuit disruptions during neonatal and perhaps adult life in patients with TSC and other genetic disorders associated with cortical malformation.

RESULTS

Neonatal *Tsc1* deletion using nestin-CreER^{T2} mice leads to olfactory lesions and the presence of enlarged neurons in the cortex

To examine whether postnatal neurogenesis contributes to olfactory lesions, we used conditional transgenic mice as recently reported to induce SVZ nodules and SEGA (41). Loss of heterozygosity in SVZ cells was achieved using mice expressing *Tsc1* alleles flanked by LoxP sites (floxed, fl) crossed with nestin-CreER^{T2}/R26R-YFP mice to generate *Tsc1*$^{fl/fl}$/nestin^{CreERT2} mice (Fig. 1A) (12,42). These nestin-CreER^{T2} mice have been used to induce selective recombination in cells of the neurogenic zones in adults (43). In neonates, nestin is also expressed in astrocytes and progressively disappears as they mature and acquire glial fibrillary acidic protein (GFAP) in rodents. Upon tamoxifen injection in *Tsc1*$^{fl/fl}$/nestin^{CreERT2}, nestin-expressing cells, including SVZ cells and astrocytes, are expected to lose *Tsc1* and express YFP. Control mice were *Tsc1*$^{fl/wt}$/nestin^{CreERT2} (wild-type, wt).

Tamoxifen was injected at P7 (two injections) and brains were collected at postnatal day (P) 28. To examine whether recombination at the *Tsc1* allele occurred, we prepared genomic DNA from the P28 cortex from *Tsc1*$^{fl/fl}$/nestin^{CreERT2} mice. We detected a *Tsc1*-mutant allele band, suggesting successful recombination ($n = 3$, Fig. 1B). In addition, as recently reported, *Tsc1*$^{fl/fl}$/nestin^{CreERT2} mice displayed GFAP- and RC2-rich SEGA-like lesions in the ventral SVZ (Fig. 1D, GFAP not shown, locations shown on the diagram in Fig. 1C) (41). RC2 is a radial glial cell marker (44).

Every *Tsc1*$^{fl/fl}$/nestin^{CreERT2} mouse displayed small YFP$^+$ lesions along the migratory tract taken by newborn neurons to reach the olfactory bulb, the rostral migratory stream (RMS) ($n = 5$, Fig. 1C and E, red circle). These lesions consisted in the accumulation of 5–20 YFP$^+$ cells that were not observed in *Tsc1*$^{fl/wt}$/nestin^{CRERT2} mice ($n = 3$, Fig. 1E). Strikingly, YFP$^+$ cells were also visible throughout the cortex in *Tsc1*$^{fl/fl}$/nestin^{CRERT2} mice (Fig. 1F), in the AON, and around the anterior commissure (data not shown). Closer examination of these cells revealed the presence of bushy cells with an astrocytic morphology and cells with a pyramidal neuron morphology (Fig. 1G for neurons). While YFP$^+$ astrocytes were also observed in the cortex of *Tsc1*$^{fl/wt}$/nestin^{CreERT2} mice, YFP$^+$ neurons were rarely detected (1–2 per section, data not shown).

These data suggest that lesions in the olfactory migratory tract can form postnatally. In addition, ectopic neurons were found in the cortex of *Tsc1*$^{fl/fl}$ mice. To identify whether cells in the lesions and the cortex were generated in the SVZ, we used an alternative approach, neonatal electroporation. This method also allows genetic manipulations of a small group of cells as opposed to global modification using transgenic mice. In addition, we used mice expressing an fl and a mutant *Tsc1* allele (*Tsc1*$^{fl/mut}$) because individuals with TSC inherit a viable and a mutant *Tsc1* (or *Tsc2*) allele. *Tsc1*$^{fl/wt}$ mice (wt for wild-type) were control littermates.

Targeted *Tsc1* removal and mTOR activation in newborn neurons via neonatal electroporation

Neonatal electroporation allows precise targeting of plasmids into neural progenitor cells lining the lateral ventricle (45). These progenitor cells generate neurons that migrate to the olfactory bulb via the RMS and are synaptically mature by 3–4 weeks after birth (46). We used *Tsc1* mice crossed with R26R-Stop-RFP mice (RFP, red fluorescent protein). In *Tsc1*$^{fl/mut}$/RFP mice, Cre recombinase (Cre) expression is expected to lead to TSC1 loss and RFP expression (Fig. 2A). RFP$^+$ neurons are thus expected to be *Tsc1*^{null} while surrounding RFP$^-$ neurons are *Tsc1*^{haplo} (haplo for haploinsufficient).

Cre- and GFP-encoding plasmid were electroporated into SVZ progenitor cells at P0–1 resulting in visible GFP fluorescence 1-day post-electroporation (Fig. 2B and C) (45,47). GFP allows to birth-mark neurons born during the first 7–10 days post-electroporation because GFP is diluted as cells divide while RFP is permanently expressed (45) (Fig. 2D). As a result, RFP$^+$ but not GFP$^+$ newborn neurons continuously accumulate in the circuit (Fig. 2E). To test for recombination at the *Tsc1* allele, we prepared genomic DNA from P7 ipsilateral (i.e. containing RFP$^+$ cells) and contralateral olfactory bulbs from *Tsc1*$^{fl/fl}$/RFP mice. A *Tsc1* mutant allele band was detected only in the ipsilateral olfactory bulb, suggesting that *Tsc1* was removed in RFP$^+$ cells ($n = 3$, Fig. 2F). Next, we performed reverse transcription polymerase chain reaction (RT-PCR) for *Tsc1* and western blot analysis from P28 olfactory bulb (OB) when *Tsc1*^{null} neurons have accumulated in the OB

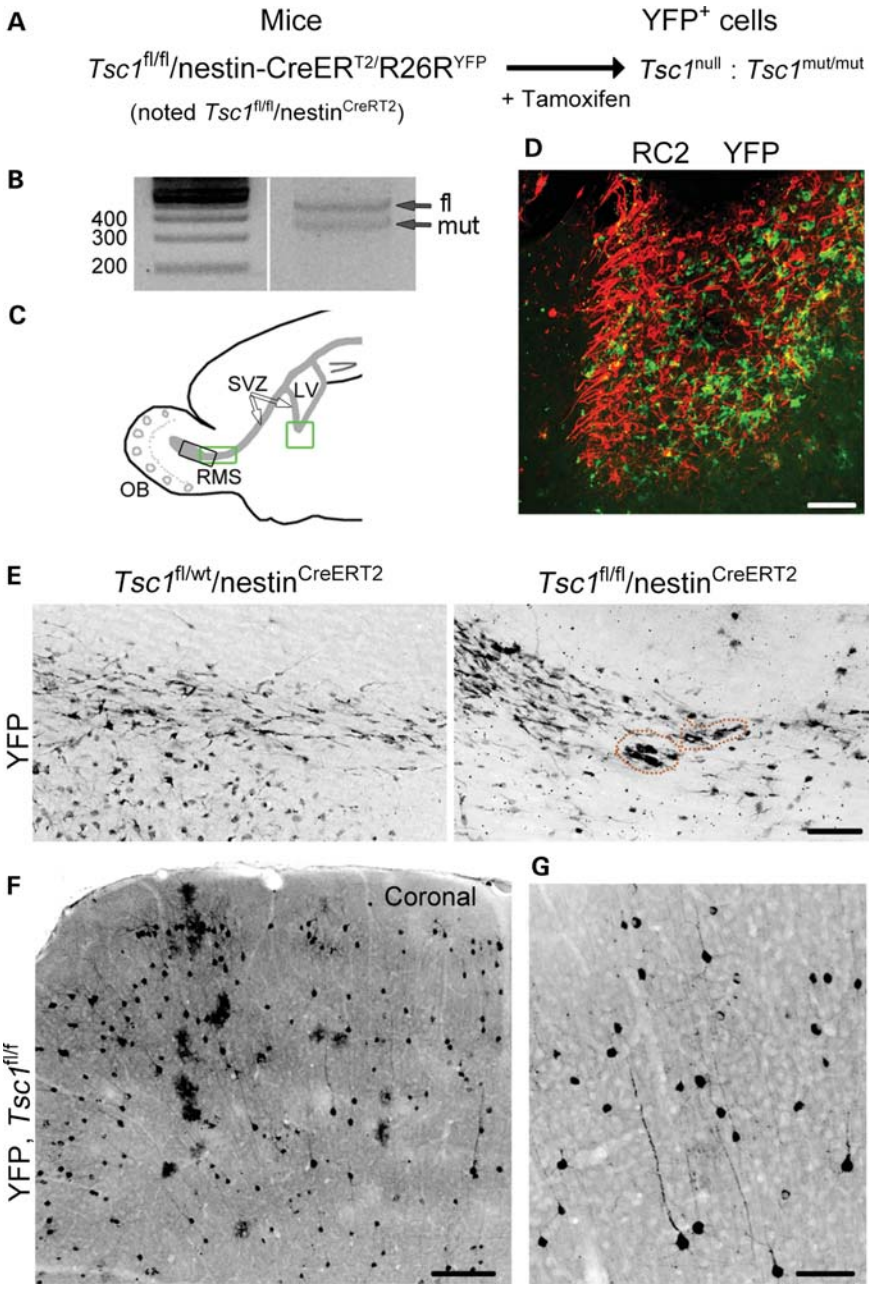

Figure 1. Postnatal deletion of *Tsc1* using inducible transgenic mice. (**A**) The diagram illustrating the inducible transgenic mouse line used to delete *Tsc1* (i.e. null) and express YFP in nestin-expressing cells and their progeny following tamoxifen injection at P7. (**B**) PCR gels from genomic DNA obtained from a P28 olfactory bulb following tamoxifen at P7. A mutant band in addition to the fl band is visible. (**C**) The diagram illustrating the locations of the images shown in (**D**) (ventral SVZ, green square) and in (**E**) (RMS, green square, for $Tsc1^{fl/fl}$ and black square for $Tsc1^{fl/wt}$) on a sagittal section. LV, lateral ventricle; SVZ, subventricular zone; OB, olfactory bulb; RMS, rostral migratory stream. (D) The P28 image of the RC2 (red)-rich SVZ nodule containing YFP^+ $Tsc1^{null}$ cells following tamoxifen-induced recombination at P7. (E) Confocal images of YFP-immunopositive cells in the RMS/RMS-OB of $Tsc1^{fl/wt}$/$nestin^{CreERT2}$ and RMS of $Tsc1^{fl/fl}$/$nestin^{CreERT2}$ following tamoxifen injections at P7. The dotted orange lines highlight small clusters of misplaced cells in the RMS. (**F** and **G**) Confocal images of YFP^+ cells (low and high magnifications) in the cortex of $Tsc1^{fl/fl}$/$nestin^{CreERT2}$ mice. Scale bars: 70 μm (D, E and G) and 200 μm (F).

for over 3 weeks, which increase our chance to detect changes in mRNA and protein levels. End-point and quantitative RT–PCR for *Tsc1* illustrated that there was a 30–40% decrease in *Tsc1* mRNA in the ipsilateral versus the contralateral $Tsc1^{fl/mut}$ olfactory bulb ($n = 3$, P28, Fig. 2G). Western blot illustrates a decrease in TSC1 (hamartin) expression in $Tsc1^{fl/mut}$ compared with $Tsc1^{fl/wt}$ ipsilateral olfactory bulbs (Fig. 2H).

mTOR hyperactivity results in elevated phosphorylation of ribosomal protein S6 (pS6) and 4E-BP. We immunostained for pS6 (Ser 240/244) in P28 olfactory bulb sections. In $Tsc1^{fl/mut}$ mice, RFP^+ neurons displayed a significant 115% increase in pS6 staining intensity compared with surrounding RFP^- neurons ($P < 0.001$, Fig. 3A–D). In contrast, 4E-BP phosphorylation was not altered (data not shown). There was

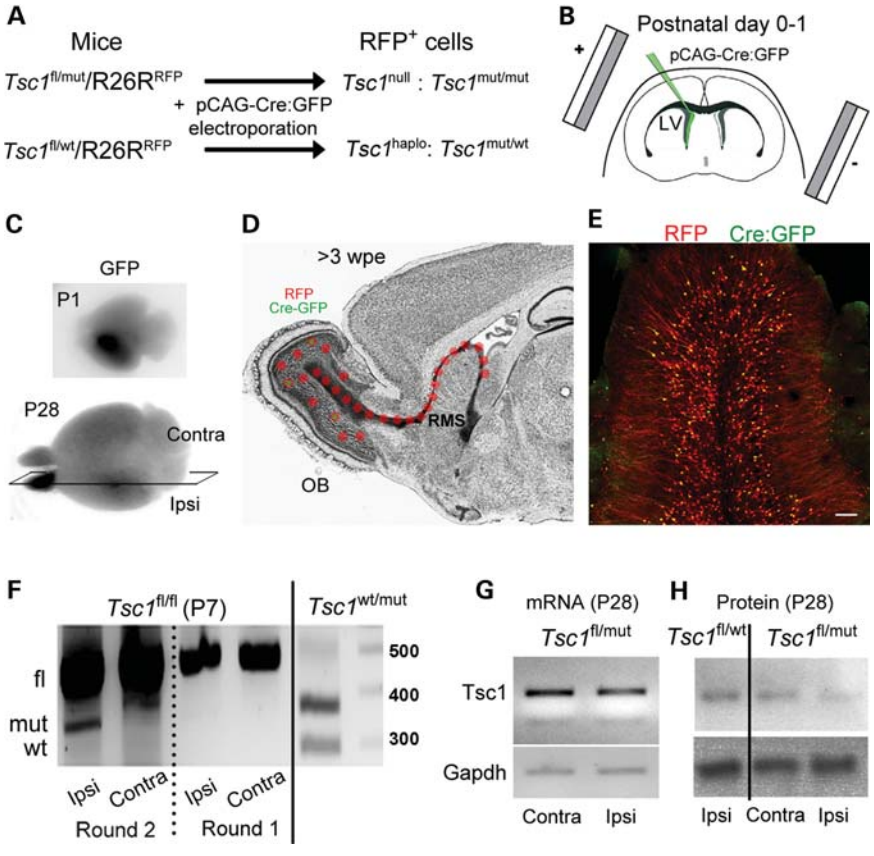

Figure 2. Postnatal deletion of *Tsc1* using neonatal electroporation and the Cre-Lox system. (**A**) Schematic describing the loss of one or two *Tsc1* alleles in cells containing a plasmid encoding Cre:GFP under the CAG promoter that is expressed through neonatal electroporation in $Tsc1^{fl/wt}$/R26R and $Tsc1^{fl/mut}$/R26R, respectively. Cells containing the pCAG-Cre:GFP also express RFP. (**B**) The diagram illustrating the principle of neonatal electroporation of a plasmid into neural progenitor cells lining the lateral ventricle. (**C**) Images of P1- and P28 fixed brains containing RFP^+ cells in the ipsilateral olfactory bulb. (**D**) The diagram illustrating the migratory path and the final location of newly born cells 3 weeks post-electroporation (wpe). RFP expression persists permanently due to its genomic integration (R26R mice), while GFP expression from either a pCAG-GFP or pCAG-Cre:GFP is diluted in newly born cells due to successive cell division. As a result, only cells born during the first 7–10 days express GFP. (**E**) The confocal image of RFP^+ and GFP^+ newly born cells in a coronal olfactory bulb section. RFP^+/GFP^+ cells outnumber RFP^+/GFP^- cells. Scale bar: 70 μm. (**F**) PCR gels from genomic DNA obtained from the ipsilateral (mRFP-containing cells) and contralateral olfactory bulb from P7 $Tsc1^{fl/fl}$/R26R and $Tsc1^{wt/mut}$/R26R mice electroporated at P1. (**G**) PCR gels of Tsc1 and Gapdh cDNA obtained from the ipsilateral and contralateral P28 $Tsc1^{fl/mut}$/R26R olfactory bulb. All the gels were run on the same blots. (**H**) Western blots of TSC1 (hamartin) and GAPDH obtained from ipsilateral P28 $Tsc1^{fl/wt}$/R26R and $Tsc1^{fl/mut}$/R26R olfactory bulbs.

no difference in pS6 staining intensity in RFP^+ compared with RFP^- neurons from $Tsc1^{fl/wt}$ mice (data not shown). Another well-known consequence of mTOR hyperactivity is an increase in cell size that was visible in $Tsc1^{null}$ neurons (Fig. 3C). RFP and 4′,6-diamidino-2-phenylindole (DAPI) counterstain were used to quantify soma and nuclei size in $Tsc1^{fl/mut}$ mice (Fig. 3E and F). RFP^+ $Tsc1^{null}$ neurons were ~3 times larger than RFP^- neurons and their nuclei 55% larger ($P < 0.001$, Fig. 3G).

Collectively, neonatal electroporation is an effective method to induce *Tsc1* deletion in newborn neurons leading to mTOR pathway activation and cytomegally.

$Tsc1^{null}$ cells form the migratory heterotopia in and out of the RMS

Gross examination of sagittal sections from P28 $Tsc1^{fl/mut}$ mice revealed the presence of the migratory heterotopia, defined by the ectopic location or misplacement of groups of $Tsc1^{null}$ cells. Examination of sagittal sections at low magnification led us identification of the heterotopia in all animals examined ($n = 13$) that were found at three major locations: in the RMS both at its entry point caudally and at the interface RMS and RMS-OB, in the RMS-OB and adjacent to the RMS in the AON as well as near the anterior commissure olfactory limb (Fig. 4A and B, black rectangles indicate the location of the heterotopia). No migratory heterotopias were visible in electroporated $Tsc1^{fl/wt}$/R26R mice (data not shown).

Closer examination of the heterotopia revealed two categories, some with an apparent mixed neuroglial phenotype (Fig. 4C–G) and some with a neuronal phenotype (Fig. 4H and I). The mixed neuroglial phenotype was visible due to the presence of a meshwork of lamelipodia-like processes giving a nodular appearance or the presence of cells with neuronal or glial morphology (Fig. 4C). Heterotopia with a lamelipodia-like structure was preferentially found in the AON as shown in Figure 4B and C. Heterotopia in the RMS and RMS-OB displayed cells with an astrocytic (bushy), a neuronal morphology or an undifferentiated morphology

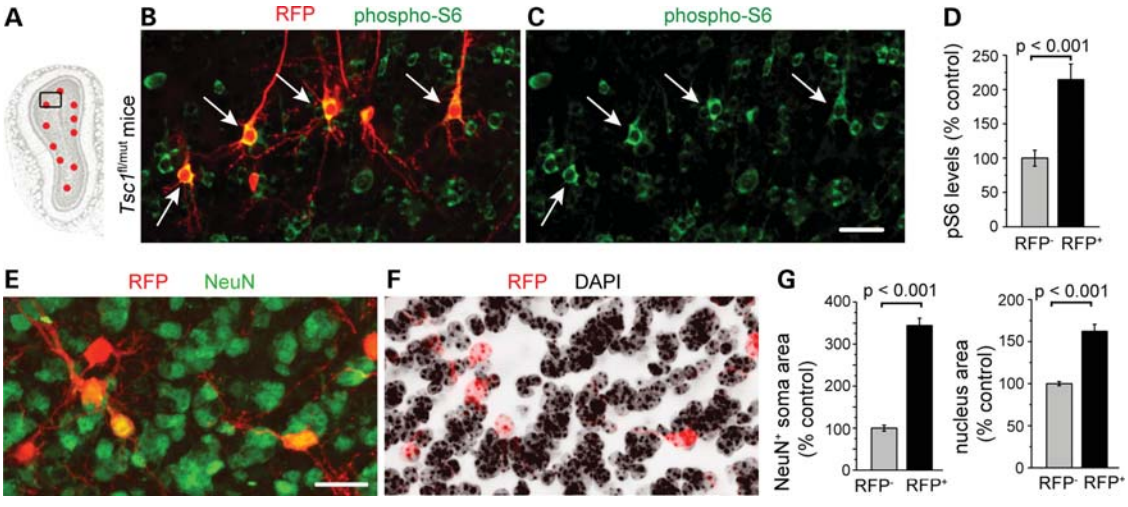

Figure 3. *Tsc1* knockout hyper-activates the mTOR pathway and leads to cytomegaly. (**A**) The diagram of a coronal olfactory bulb section with the black square indicating the approximate location of the image in (**B**) and (**C**). (B and C) Confocal images of RFP fluorescence (red) and phospho-S6 immunostaining (green). Arrows point to neurons with an enlarged pS6 soma. (**D**) The bar graph of the pS6 intensity of all RFP^+ neurons as a % of control RFP^- neurons (mean ± SEM, *t*-test). (**E** and **F**) Confocal images of RFP fluorescence (red) and NeuN immunostaining (green, E) and DAPI counterstain (black, F). (**G**) Bar graphs of the $NeuN^+$ soma area and the nuclear area as a % of control. Scale bars: 30 μm (B and C) and 20 μm (E and F).

(Fig. 4D–G). Some cells stained for the astrocytic marker GFAP (data not shown). Cells with a neuronal morphology displayed extensive dendrites with spines and a thin process identified as an axon by the presence of varicosities (white arrows, Fig. 4E–G). Cells forming the heterotopia displayed enlarged cells body compared with surrounding cells, in particular doublecortin (DCX)-immunopositive neuroblasts in the RMS (Fig. 4F and G, DCX staining not shown).

Mixed phenotype–heterotopia comprised GFP^+ and GFP^-/RFP^+ cells. In wt mice, GFP^+ cells, which are born between P0 and P10, should have reached the olfactory bulb by P28 (see 45 for more details). Indeed in $Tsc1^{fl/wt}$/R26R mice, only 8% of the RFP^+ cells were GFP^+ in the RMS (23/250 cells, $n = 3$ mice). In contrast, we found that 22% of $Tsc1^{null}$ RFP^+ cells were GFP^+ cells in the RMS (280/1092 cells, $n = 3$, $P < 0.0001$, Fisher's exact test). Thus, heterotopia contained early born GFP^+ cells that are stalled in the RMS and may thus trap late born cells as well as disrupt their migratory path.

Heterotopia comprised of 3–15 cytomegalic neurons is also visible along the RMS-OB and more specifically, in the anterior commissure olfactory limb (Fig. 4H and I). These cells displayed a neuronal morphology and were NeuN and pS6 immunopositive (data not shown). The majority of these ectopic neurons were GFP^+ and thus early born (Fig. 4H).

Tsc1^{null} cells in the RMS display abnormal morphology and are slow or stalled

Outside the heterotopia, the RMS of P28 $Tsc1^{fl/mut}$/R26R mice appeared more disorganized compared with that of $Tsc1^{fl/wt}$/R26R mice (Fig. 5A and B). This appearance was due to the presence of cells with a more complex morphology and enlarged soma scattered along the RMS (arrows, Fig. 5B). As a mean, $Tsc1^{null}$ cells had one more process than $Tsc1^{haplo}$ cells (a mean of 2.2 ± 0.2 versus 1.4 ± 0.1, $P < 0.05$, Fig. 5C). Complex $Tsc1^{null}$ cells were DCX^-, while morphologically simpler cells were DCX^+ identifying them as neuroblasts (data not shown).

Next, we performed a migration assay in acute sagittal slices from the RMS of P21 mice (45,47). $Tsc1^{haplo}$ neuroblasts migrated at a 54.4 ± 2.2 μm/h, which is similar to a previously reported value for neuroblast migration in wt mice (47–49). $Tsc1^{null}$ neuroblasts migrated at 37.1 ± 2.5 μm/h and were thus 33% slower than $Tsc1^{haplo}$ cells (128 and 83 cells, $P < 0.0001$, Fig. 5D). $Tsc1^{null}$ cells with a complex morphology were stationary.

We also found scattered $Tsc1^{null}$ giant cells characterized by a soma size 3–4 times larger than that of other $Tsc1^{null}$ cells (Fig. 5E). These cells had a disheveled morphology, were NeuN negative and contain multiple nuclei (Fig. 5E–G). Two nuclei can be appreciated in Figure 5G and H. A mean of five giant cells were found per RMS of $Tsc1^{fl/mut}$/R26R mice, while none was seen in the RMS of $Tsc1^{fl/wt}$/R26R mice.

Micronodules throughout the olfactory bulb containing neurons with a hypertrophic dendritic tree

Upon entering the olfactory bulb, the majority of newborn neurons integrate in the granule cell layer. Ultimate circuit formation depends on proper cell placement and morphogenesis. We thus examined the overall organization of granule cells and their dendritic arbor. In coronal olfactory bulb sections, the overall cell distribution was disrupted in $Tsc1^{fl/mut}$/R26R compared with $Tsc1^{fl/wt}$/R26R mice (Fig. 6A and B). This is in addition to obvious increase in the size of $Tsc1^{null}$ cells as measured in Figure 2. Perhaps, more visible in sagittal sections was the apparent clumping of cytomegalic $Tsc1^{null}$ cells (Fig. 6D), while $Tsc1^{haplo}$ cells were equally distributed (Fig. 6C). To quantify the disorganization of granule cells, we performed nearest neighbor calculations in which the

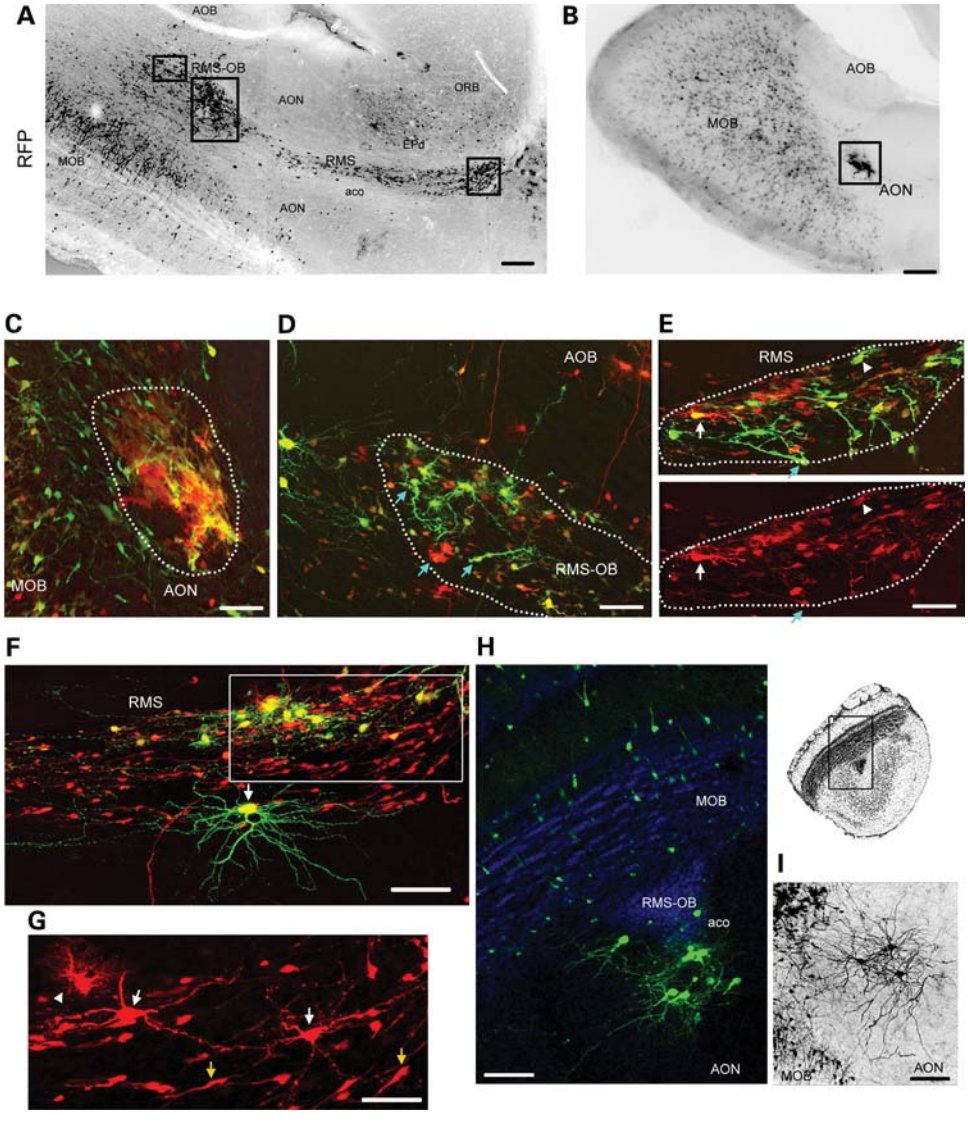

Figure 4. *Tsc1*^{null} cells form the migratory heterotopia in and out of the RMS. Low magnification photographs of RMS/RMS-OB (**A**) and AON (**B**) lesions containing RFP^{+} cells in sagittal sections of *Tsc1*$^{fl/mut}$/R26R mice electroporated at P1 with pCAG-Cre:GFP and pCAG-GFP. The black rectangles illustrate the approximate locations of images shown in (**C**)–(**E**). (C) The confocal image of a lesion in the AON, the location of which is shown in (B). The lesion contains RFP^{+}/GFP^{+} and RFP^{+}/GFP^{-} cells. (D–**G**) Confocal Z-stack images of lesions in the RMS-OB (D) and RMS (E and F), the locations of which are shown in (A). G is a zoom and smaller Z-stack of the region in the white rectangle in F. Blue arrows (D and E) point to cells with an immature morphology. White arrows (E, F and G) point to some neurons. The arrowhead (E and G) points to examples of cells resembling astrocytes. Yellow arrows (in G) point to neuroblasts. (**H** and **I**) Confocal Z-stack images of neuronal heterotopias in the aco of the olfactory bulb in a coronal section (GFP^{+} neurons in green and DAPI in blue, H) and the neuronal heterotopia in the AON (black, I). Scale bars: 700 μm (A and B), 40 μm (C), 35 μm (D), 50 μm (E and G) and 70 μm (F, H and I). aco, anterior commissure, olfactory limb; AOB, accessory olfactory bulb; AON, accessory olfactory nucleus; aco:EP, doral endopiriform cortex; ORB, orbital cortex.

density of cells and the distance between each were measured (Fig. 6E). These measurements were compared with a theoretical Poisson distribution. The difference between the theoretical and experimental values in *Tsc1*$^{fl/mut}$/R26R mice was significantly lower than that in *Tsc1*$^{fl/wt}$/R26R mice ($R = 4.2 \pm 1.2$, $n = 10$ versus $R = 9.0 \pm 1.5$, $n = 12$ sections, Fig. 6F), suggesting a decreased organization in the *Tsc1*$^{fl/mut}$ olfactory bulb ($P < 0.05$).

Another observation in coronal sections was the hypertrophic dendritic tree of *Tsc1*^{null} granule neurons (Fig. 7A). Using Scholl analysis of the proximal dendrites, we found that the number of dendritic crossings was increased in *Tsc1*^{null} compared with *Tsc1*^{haplo} neurons (Fig. 7B).

Newborn neurons are rerouted to cortical and subcortical areas

Considering that cortical neurons were observed in the *Tsc1*$^{fl/fl}$/nestin^{CreRT2}, we examined for the presence of neurons in cortical and subcortical structures in coronal sections. In all *Tsc1*$^{fl/mut}$ brains examined, we found GFP^{+} neurons in the nucleus accumbens and in the cortex (Fig. 8). The majority of neurons were GFP^{+} suggesting that they were born during the neonatal period. Such neurons were absent in the Tsc1$^{fl/wt}$ brain or very rare (1 per section occasionally). In the nucleus accumbens, neurons were located at the base of the lateral ventricle and around the anterior commissure

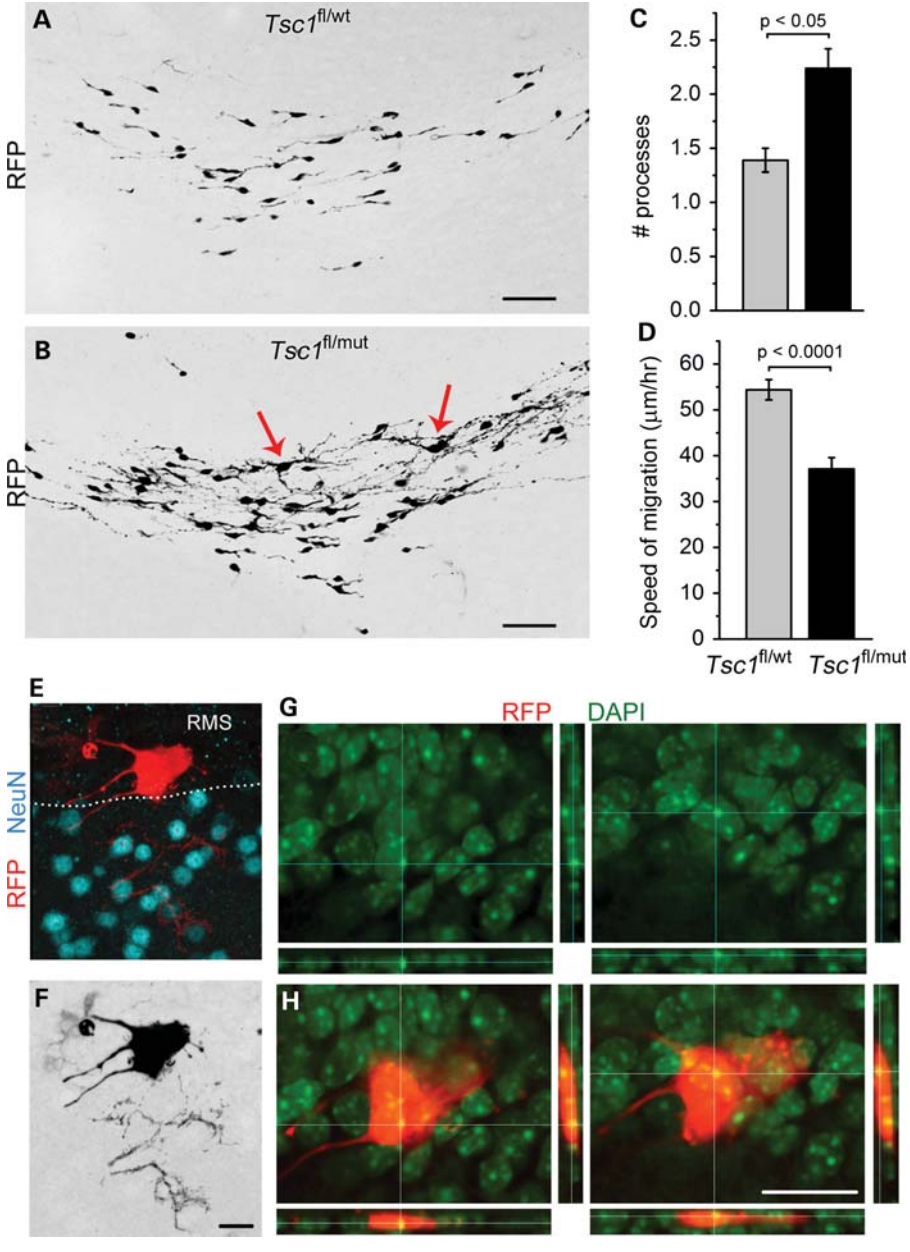

Figure 5. *Tsc1*^{null} cells in the RMS display a hypertrophic morphology and are slow. (**A** and **B**) Confocal Z-stack images of RFP^{+} cells in the RMS of *Tsc1*$^{fl/wt}$/R26R and *Tsc1*$^{fl/mut}$/R26R mice. Bar graphs of the number of processes (**C**) and the speed of RFP+ cell migration (**D**) in *Tsc1*$^{fl/wt}$/R26R (gray) and *Tsc1*$^{fl/mut}$/R26R (black). (**E**) The confocal image of an enlarged RFP^{+} cells (red) and NeuN immunostaining (blue) in the RMS sending a process in the accessory olfactory nucleus. (**F**) The same cell as in (E) in black and white. (**G** and **H**) Projections from the same RFP^{+} cell (red) as in (E) and DAPI counterstain (green, alone in G) to illustrate the presence of two nuclei. Scale bars: 50 μm (A and B), 30 μm (F) and 40 μm (G).

(Fig. 8B and C). GFP^{+} cells were identified as neurons based on NeuN immunostaining. In the cortex, 10–15 neurons were found per sections. Neurons occurred in clusters of 2–6 and were located in the deep cortical layers and in layer II (Fig. 8D–I). Cortical neurons display an extensive dendritic tree with spines as well as a thin process with varicosities resembling an axon.

DISCUSSION

Here, we show that focal *Tsc1* knockout in the postnatal SVZ results in mTOR pathway activation and migratory alterations characterized by the heterotopia along the migratory path, olfactory bulb disorganization and neuronal misrouting to cortical and subcortical structures. In addition, newborn *Tsc1*^{null} neurons displayed a reduced migration rate and an enhanced dendritic tree.

To explore whether postnatal neurogenesis contributed to some of the lesions observed in TSC patients, we used two strategies. First, we used inducible transgenic mice, in which tamoxifen injections led to *Tsc1* loss in nestin-expressing cells, including SVZ cells. This resulted in the formation of SEGA-like lesions as reported recently (41). In addition, we found small heterotopias (i.e. clusters of misplaced cells)

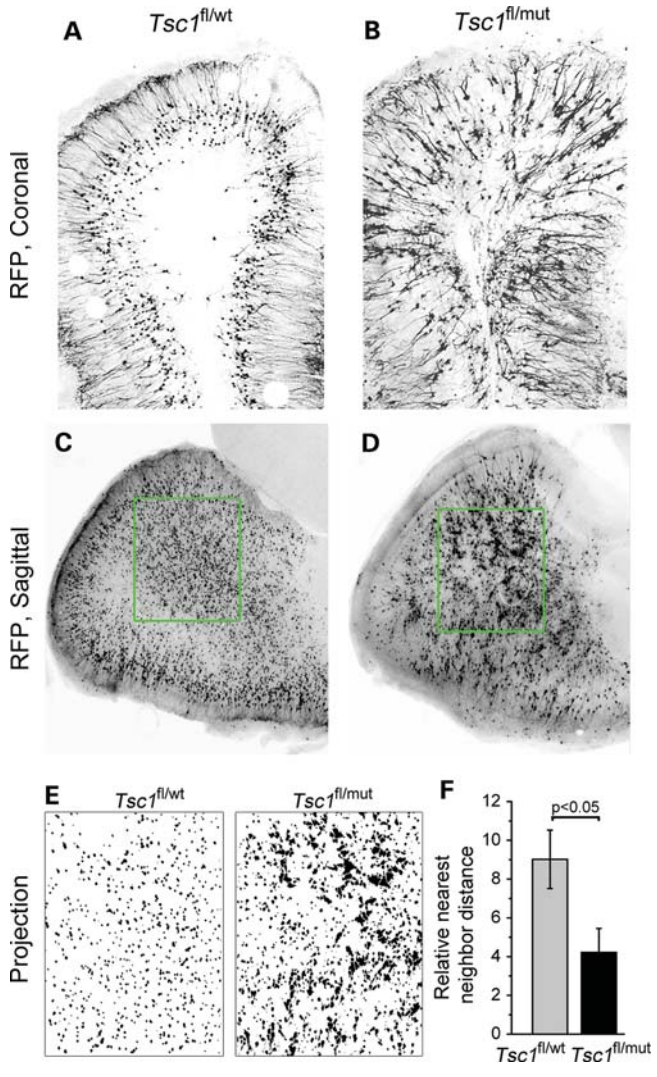

Figure 6. *Tsc1*^{null} neurons form micronodules throughout the olfactory bulb. Confocal images of RFP^{+} cells in olfactory bulb coronal (**A** and **B**) and sagittal (**C** and **D**) sections from *Tsc1*$^{fl/wt}$/R26R (A and C) and *Tsc1*$^{fl/mut}$/R26R mice (B and D). (**E**) Projections of the RFP signals in the green square in (C) and (D). (**F**) The bar graph of the relative nearest neighbor distance for RFP^{+} cells in the olfactory bulb of *Tsc1*$^{fl/wt}$/R26R (gray) and *Tsc1*$^{fl/mut}$/R26R (black) mice. Scale bars: 140 μm (A and B) and 200 μm (C and D).

along the RMS and the presence of neurons in the cortex that were absent in control mice. Although this strategy is efficient, it does not unambiguously identify SVZ cells as the source of the ectopic neurons and heterotopia. Second, we thus used *in vivo* electroporation to express Cre- and GFP-encoding plasmids selectively in SVZ cells resulting in *Tsc1* deletion when using *Tsc1*$^{fl/mut}$ mice. It is worth emphasizing that patients are born heterozygote for *Tsc1* or *Tsc2*. However, the heterozygote mice do not display any gross abnormalities (50). Considering that the SEGA in the SVZ have lost heterozygosity in TS patients (51), some of the cells generated from the SVZ are expected to be *Tsc1*^{null} or *Tsc2*^{null}. The following data emphasize that loss of heterozygosity is necessary for lesion formation.

Following *Tsc1* removal in neonatal neural progenitor cells and thus their progeny, we identified lesions as reported in TSC patients, in particular the heterotopias commonly called olfactory hamartomas (32,33). These heterotopias had either a mixed neuroglial or neuronal phenotype. The neuronal heterotopias contained cytomegalic, spiny neurons with enhanced mTOR activity and the presence of axons. The majority of these neurons were GFP^{+}, suggesting that they were born during the neonatal period (P1–10). The mixed neuroglial heterotopia contained a mixture of early born GFP^{+}/RFP^{+} cells and GFP^{-}/RFP^{+} cells born ∼3–7 days prior to preparing brain sections (P28). These data suggest that the continual generation of cells from *Tsc1*^{null} SVZ neural progenitor cells leads to progressive accumulation of cells in the lesions and their subsequent increase in size. It remains unclear why some cells remains stalled along the migratory path. A premature differentiation as seen by the presence of cells with astrocytic and neuronal morphology could result in cell immobility. Alternatively, the presence of immature-looking cells with a radial-like morphology suggests that neural progenitor cells (i.e. radial glial cells) did not fully differentiate and remain stalled in the SVZ. Addressing this issue is outside the scope of this study. During migration, *Tsc1*^{null} neuroblasts displayed a slowed migration speed and a more complex morphology than *Tsc1*^{haplo} neuroblasts. Once in the olfactory bulb, *Tsc1*^{null} neurons formed micronodules, suggesting that their positional cues were altered. In addition, they displayed a hypertrophic dendritic tree consistent with a role of the mTOR pathway on dendritogenesis (52).

Another major finding is the presence of GFP^{+} neurons in the cortex and nucleus accumbens around the anterior commissure. Cortical neurons were spiny and displayed morphologies reminiscent of pyramidal neurons. They also exhibited a thin process resembling an axon. Although only 10–15 were found per slice, they clustered in groups of 2–6 and could have a major impact on local circuit function. The function of these ectopic neurons will clearly warrant further investigation.

Our findings have major implications and raise important new questions. It is highly conceivable that *Tsc1*^{null} cells born along the SVZ around the time of birth in humans (neonatal period in mice) can generate olfactory lesions. In addition, because neural stem cells and neurogenesis persist in juvenile and adult humans (19,20,28), the continual generation of *Tsc1*^{null} cells from the SVZ in TSC patients may feed and increase in size the lesions that are formed neonatally or embryonically. Finding micronodules in the olfactory bulb raises the possibility that such abnormal structures may also be generated during embryonic life and would not be visible through conventional imaging. This finding together with the presence of ectopic neurons in the cortex and subcortical regions calls for closer examination of TSC tissue outside the tubers. Finally, TSC shares histological and clinical features with other disorders of cortical malformations such as focal cortical dysplasia and ganglioma that are associated with defects in neurogenesis (22). Collectively, we thus propose that neurogenesis along the SVZ progressively contributes to alterations in the forebrain during the neonatal and juvenile period resulting in progressive circuit disruption and perhaps neuropsychiatric instability in patients with TSC and other cortical malformations.

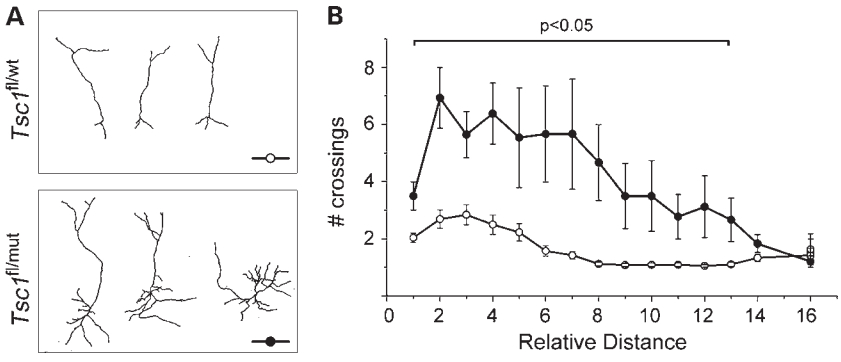

Figure 7. *Tsc1*^{null} neurons display a hypertrophic dendritic tree. (**A**) Representative reconstructions of RFP^{+} olfactory neurons in sections from *Tsc1*$^{fl/wt}$/R26R and *Tsc1*$^{fl/mut}$/R26R mice. (**B**) Corresponding plots of the number of crossing as a function of the distance from the soma ($n = 14$ cells for each plot). Filled circles: *Tsc1*$^{fl/mut}$/R26R mice.

MATERIALS AND METHODS

Animals

Research protocols were approved by the Yale University Institutional Animal Care and Use Committee. Experiments were performed on littermate *Tsc1*$^{fl/wt}$/R26R and *Tsc1*$^{fl/mut}$/R26R mice obtained by crossing the following two lines of transgenic mice: *Tsc1*$^{fl/fl}$ (Jackson Laboratories) and *Ts1*$^{wt/mut}$ (NCI) that we had crossed with R26R-Stop-RFP mice (Jackson Laboratories, RFP for tdTomato). These two lines of mice were generated by David J. Kwiatkowski (Brigham and Women's Hospital, Harvard Medical School, Cambridge, MA, USA). For additional experiments, *Tsc1*$^{fl/fl}$ mice were crossed with nestin-CreER^{T2} mice (kind gift from Dr Amelia Eisch, UT Southwestern) that we had crossed with R26R-Stop-YFP mice (Jackson Laboratories) to generate *Tsc1*$^{fl/fl}$/nestin^{CreERT2} mice. Mice were prescreened for successful electroporation prior to sacrificing by viewing with an epifluorescence microscope or a Kodak 4000 imager.

Genotyping

Tail or toe samples were prepared using the standard protocols. We used previously published primers (53,54). The primer combination allows for the detection of the wt *Tsc1* allele at 295 bp, the fl allele at 480 bp and the mutant allele at 370 bp. The fl allele contains the LoxP sites surrounding the sequence to be excised upon Cre recombination. The mutant allele lacks the sequence flanked by LoxP sites, thus making the hamartin protein non-functional.

Neonatal electroporation

Electroporation is as we described previously (45,47). Plasmids (2–3 μg/μl) were diluted in phosphate buffered saline containing 0.1% fast green as a tracer; 0.5–1 μl of plasmid solution was injected into the lateral ventricles of cold-anesthetized neonatal pups using a pulled glass pipette (diameter <50 μm). Five square pulses of 50 ms duration with 950 ms intervals at 100 V were applied using a pulse ECM830 BTX generator and tweezer-type electrodes (model 520, BTX) placed on the heads of P0–1 pups.

Microdissection, RNA extraction and RT–PCR

Trizol reagent (750 μl) plus 200 μl of chloroform were added to each olfactory bulb sample and passed through a 22-gauge 1.5-inch needle and then vortexed. Following centrifugation for 15 min at 4°C and 12 000 *g*, the top aqueous phase was transferred to a fresh reaction tube. After adding 1000 μl of ethanol, the sample was vortexed for 1 min and centrifuged at 8000 *g* for 15 s. Pellets were rinsed three times with 75% ethanol. Following centrifugation, the RNA was eluted with RNase-free deionized H_2O prior to determining its concentration and purity on a spectrophotometer. The samples with contamination were subjected to an additional ethanol/sodium acetate precipitation.

For reverse transcription polymerase chain reaction (RT-PCR), 2.12 μg of RNA was mixed with deoxynucleotide triphosphates (dNTPs), random primers (Invitrogen) and RNase/DNase-free deionized H_2O, heated for 5 min at 65°C and then rapidly chilled on wet ice for 5 min, followed by brief centrifugation. Dithiothreitol, RNase out and SuperScript III were then added to each sample and reverse transcribed in a BioRad MyCycler. cDNA was then subjected to PCR using primers to *Tsc1* and *Gapdh*. Primer sequences are available upon request. mRNA transcripts were quantified by the standard curve method of qRT–PCR. cDNA was amplified with the specified primers and detected with SYBR Green (Bio-Rad) by a Chromogen-modified iCycler.

Genomic DNA isolation

Fresh, unfixed tissue was subjected to a proteinase K dilution and genomic DNA isolated using a DNeasy kit (DNA extraction). Quantification of DNA purity and concentration was performed, and ~0.19 μg of DNA was added to PCRs. 10× PCR buffer (Invitrogen) was added to 10 mM dNTP mix, 50 mM $MgSO_4$, autoclaved DNase-free deionized H_2O and Platinum Taq. The reaction volume was 25 μl after adding 1 μl of each forward and reverse primer with 3 μl of the appropriate sample. PCR was performed in a BioRad MyCycler (32–36 cycles). For recombination detection, 5 μl of product was subjected to a second round of PCR. Amplicons were visualized by running samples diluted in 10× blue juice DNA loading buffer loaded onto a 2% agarose gel run at 100 V for 30 min alongside a 100-bp DNA ladder (Invitrogen).

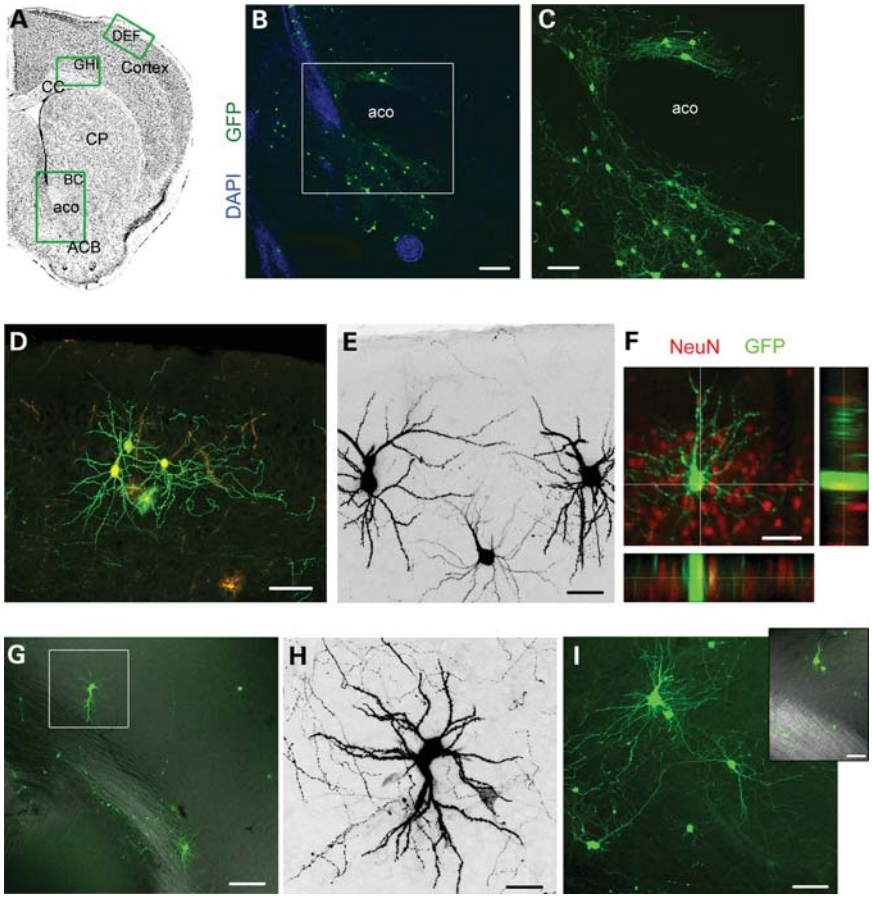

Figure 8. Newborn *Tsc1*^{null} neurons are rerouted to cortical and subcortical areas. (**A**) Coronal sections with green rectangles indicating the approximate locations of images shown in (**B**)–(**I**). (B) The confocal image of GFP^{+} neurons (green) in the ACB and around the aco counterstained with DAPI (blue). (C) The zoom of the image in the white square in (B). (D) The confocal image of GFP^{+} and RFP^{+} neurons and astrocytes (bushy cells) in cortical layer II. (E) GFP^{+} (black) neurons in cortical layer II. (F) The confocal image and projections of a GFP^{+} cortical layer II cell that immunostained positive for NeuN (red). (G) The confocal image of GFP^{+} neuron in the deep layer of the cortex. (H) Zoom of the neuron in the white square in (G). (I) The confocal image of GFP^{+} neuron in the deep layer of the cortex. Inset: GFP fluorescence overlaid with DIC to illustrate the location of the corpus callosum. CC, corpus callosum; CP, caudate putamen; ACB, accumbens nucleus; aco, anterior commissure. Scale bars: 140 μm (B) 70 μm (C), 80 μm (D and G), 40 μm (E, F and I) and 30 μm (H).

Slice preparation and immunostaining

P28 mice were deeply anesthetized with pentobarbital (50 mg/kg). The brain was then quickly removed and placed in 4% paraformaldehyde overnight at 4°C, then washed in 1× PBS. The region of electroporation was imaged using a Kodak 4000 imager. The next day, 100-μm-thick slices were prepared using a vibratome (Leica VTS 1000). Immunostaining was performed in free-floating 100-μm-thick slices as described previously (55). Free-floating sections were blocked in PBS containing 0.1% Triton X-100, 0.1% Tween-20 and 2% bovine serum albumin and incubated in primary antibodies (see below) overnight at 4°C. After several washes in PBS containing 0.1% Tween-20, slices were incubated with the appropriate secondary antibody [Alexa Fluor series at 1:1000 (Invitrogen) or Cyanine series at 1:500 (Jackson ImmunoResearch)] for 1 h at room temperature. Primary antibodies were rabbit anti-pS6 (1:1000; Cell Signaling; S235/236, 2F9, catalog #4856), mouse anti-NeuN (1:500; Millipore), GFAP (1:100, DAKO) and DCX (1:500, Santa Cruz Biotechnology). Each staining was replicated in slices from three different mice. Z-section images were acquired on a confocal microscope (Olympus FluoView 1000) with a 20× dry objective (N.A. 0.75). Low-magnification images were acquired with a 10× dry objective or a dissecting scope (SZX16 with a SDF PLAPO 1× PF objective). Images were analyzed using Imaris 4.0 (Bitplane AG) and reconstructed using ImageJ 1.39t software (Wayne Rasband, NIH) or Photoshop CS3.

Cell size and pS6 immunostaining analyses

To measure cell size, Z-stack images of mRFP^{+} cells in coronal sections were acquired with a 20× dry objective (Numerical Aperture, 0.75) using high–low settings to minimize saturation. In ImageJ, the freehand tracing tool was used to outline cell somas. Cell size was represented relative to the indicated controls. To measure nuclear size, Z-stack images of coronal sections stained for NeuN and DAPI were acquired with a 40× dry objective (Numerical Aperture, 1.20). Likewise, the freehand tracing tool was used to outline neuronal nuclei.

To measure mTOR activity, immunostaining was performed using an antibody to phosphorylated serine 235/236 of pS6. Serial Z-stacks were acquired under the same settings for the

ipsilateral and contralateral coronal sections of an olfactory bulb. Regions of interest (ROIs) were generated using an elliptical selection tool, and average intensities for each ROI were determined. For both cell size and pS6 staining measurement, three sections per mouse were analyzed.

Acute slice migration assays

P21 mice were deeply anesthetized 20 mg/kg Nembutal and brains were dissected into ice-cold, oxygenated (95% O_2, 5% CO_2) high-glucose Dulbecco's modified eagle medium (DMEM). The 300 μm-thick sagittal slices were obtained using a Leica vibratome. After incubating for 1 h in room temperature DMEM, slices were transferred to a heated (35°C) perfusion chamber for 1 h. Individual fluorescently labeled cells in the RMS or RMS-OB were visualized using a confocal Olympus FluoView 1000 system. Confocal Z-stack images (4 μm spaced sections over 60–100 μm) were acquired with a 20× immersion objective (XUMPLFL, N.A. 1.20) every 5 min for at least 90 min. Movies were analyzed in ImageJ software (NIH). Image stacks were realigned and RFP-fluorescent cells were tracked using ImageJ plug-ins [Stackreg (56) and MTrackJ written by Dr E. Meijering, Biomedical Imaging Group Rotterdam]. Individual fluorescent cells were tracked using the MTrackJ plug-in. Cell migration speeds were calculated with a macro program as described previously (47,48).

Olfactory bulb organization

Sagittal slices were optically sectioned in the Z-plane at 4 μM intervals at a 4× magnification. Sections were stacked and converted to an 8-bit digital image followed by binary watershedding in ImageJ. Images were loaded and processed in geological image analysis software (GIAS v1.12, Beggan and Hamilton, 2010). Default settings were applied, and the nearest neighbor distance Ra was calculated. Organization is then measured as the theoretical Ra (based on a Poisson distribution) minus experimental Ra.

Morphometric analysis

Complete images of RFP^+ neurons were acquired in coronal sections using a Fluoview 1000 confocal microscope and 20× objective with a 2× digital zoom to focus on basal neurites. Neurites were traced with simple neurite tracer software (FIJI, GNU GPL v3). Scholl analyses were carried out using dendrite length as a measure of morphological complexity. Confocal Z-stacks from three different square fields of view were taken from each olfactory bulb section, and this was done for three different OB sections in a randomly selected series from each animal. At least three animals were analyzed per condition.

Statistics

Analysis of cell size and pS6 was performed on an average of 20–25 cells per slice, respectively, from 3 to 4 animals in each condition. The laminar distribution of cells was performed on 1–2 slices for 3–4 animals of each genotype. Data were presented in Origin 8.0. Statistical significance was determined using the unpaired Student's *t*-test or the Fisher's exact test when mentioned with $P < 0.05$ for significance (KyPlot 2.0). Data are presented as the mean ± SEM.

ACKNOWLEDGEMENTS

We thank Dr Amelia Eisch (UT Southwestern) for kindly providing the nestin-$CreER^{T2}$ mice and Tiffany Lin for advice on using FIJI. The images of coronal brain sections were obtained from the Allen Brain Atlas.

Conflict of Interest statement. None declared.

FUNDING

This work was supported by grants from the Department of Defense (DoD, A.B.), a National Institutes of Health NRSA (grant number 10668225) and Epilepsy Foundation fellowship (D.M.F.).

REFERENCES

1. Osborne, J.P., Fryer, A. and Webb, D. (1991) Epidemiology of tuberous sclerosis. *Ann. N. Y. Acad. Sci.*, **615**, 125–127.
2. European Chromosome 16 Tuberous Sclerosis Consortium. (1993) Identification and characterization of the tuberous sclerosis gene on chromosome 16. *Cell*, **75**, 1305–1315.
3. Curatolo, P., Seri, S., Verdecchia, M. and Bombardieri, R. (2001) Infantile spasms in tuberous sclerosis complex. *Brain Dev.*, **23**, 502–507.
4. Holmes, G.L. and Stafstrom, C.E. (2007) Tuberous sclerosis complex and epilepsy: recent developments and future challenges. *Epilepsia*, **48**, 617–630.
5. Webb, D.W., Fryer, A.E. and Osborne, J.P. (1996) Morbidity associated with tuberous sclerosis: a population study. *Dev. Med. Child Neurol.*, **38**, 146–155.
6. Weiner, D.M., Ewalt, D.H., Roach, E.S. and Hensle, T.W. (1998) The tuberous sclerosis complex: a comprehensive review. *J. Am. Coll. Surg.*, **187**, 548–561.
7. Crino, P.B. (2004) Molecular pathogenesis of tuber formation in tuberous sclerosis complex. *J. Child Neurol.*, **19**, 716–725.
8. Crino, P.B., Aronica, E., Baltuch, G. and Nathanson, K.L. (2010) Biallelic TSC gene inactivation in tuberous sclerosis complex. *Neurology*, **74**, 1716–1723.
9. Feliciano, D.M., Su, T., Lopez, J., Platel, J.C. and Bordey, A. (2011) Single-cell Tsc1 knockout during corticogenesis generates tuber-like lesions and reduces seizure threshold in mice. *J. Clin. Invest.*, **121**, 1596–1607.
10. Thiele, E.A. (2004) Managing epilepsy in tuberous sclerosis complex. *J. Child Neurol.*, **19**, 680–686.
11. Uhlmann, E.J., Wong, M., Baldwin, R.L., Bajenaru, M.L., Onda, H., Kwiatkowski, D.J., Yamada, K. and Gutmann, D.H. (2002) Astrocyte-specific TSC1 conditional knockout mice exhibit abnormal neuronal organization and seizures. *Ann. Neurol.*, **52**, 285–296.
12. Meikle, L., Talos, D.M., Onda, H., Pollizzi, K., Rotenberg, A., Sahin, M., Jensen, F.E. and Kwiatkowski, D.J. (2007) A mouse model of tuberous sclerosis: neuronal loss of Tsc1 causes dysplastic and ectopic neurons, reduced myelination, seizure activity, and limited survival. *J. Neurosci.*, **27**, 5546–5558.
13. Way, S.W., McKenna, J. III, Mietzsch, U., Reith, R.M., Wu, H.C. and Gambello, M.J. (2009) Loss of Tsc2 in radial glia models the brain pathology of tuberous sclerosis complex in the mouse. *Hum. Mol. Genet.*, **7**, 1252–1265.
14. Zeng, L.H., Rensing, N.R., Zhang, B., Gutmann, D.H., Gambello, M.J. and Wong, M. (2010) Tsc2 gene inactivation causes a more severe epilepsy phenotype than Tsc1 inactivation in a mouse model of tuberous sclerosis complex. *Hum. Mol. Genet.*, **3**, 445–454.

15. Choi, Y.J., Di Nardo, A., Kramvis, I., Meikle, L., Kwiatkowski, D.J., Sahin, M. and He, X. (2008) Tuberous sclerosis complex proteins control axon formation. *Genes Dev.*, **22**, 2485–2495.
16. Mizuguchi, M. and Takashima, S. (2001) Neuropathology of tuberous sclerosis. *Brain Dev.*, **23**, 508–515.
17. Wei, J., Li, P., Chiriboga, L., Mizuguchi, M., Yee, H., Miller, D.C. and Greco, M.A. (2002) Tuberous sclerosis in a 19-week fetus: immunohistochemical and molecular study of hamartin and tuberin. *Pediatr. Dev. Pathol.*, **5**, 448–464.
18. Eriksson, P.S., Perfilieva, E., Bjork-Eriksson, T., Alborn, A.M., Nordborg, C., Peterson, D.A. and Gage, F.H. (1998) Neurogenesis in the adult human hippocampus. *Nat. Med.*, **4**, 1313–1317.
19. Curtis, M.A., Kam, M., Nannmark, U., Anderson, M.F., Axell, M.Z., Wikkelso, C., Holtas, S., Roon-Mom, W.M., Bjork-Eriksson, T., Nordborg, C. *et al.* (2007) Human neuroblasts migrate to the olfactory bulb via a lateral ventricular extension. *Science*, **315**, 1243–1249.
20. Wang, C., Liu, F., Liu, Y.Y., Zhao, C.H., You, Y., Wang, L., Zhang, J., Wei, B., Ma, T., Zhang, Q. *et al.* (2011) Identification and characterization of neuroblasts in the subventricular zone and rostral migratory stream of the adult human brain. *Cell Res.*, **11**, 1534–1150.
21. Zhao, C., Deng, W. and Gage, F.H. (2008) Mechanisms and functional implications of adult neurogenesis. *Cell*, **132**, 645–660.
22. Bordey, A. (2009) Neonatal progenitor contribution to epilepsy-associated cortical malformations. In Schwartzkroin, P.A. (ed.), *Encyclopedia of Basic Epilepsy Research*. Elsevier, Boston.
23. Pathania, M., Yan, L.D. and Bordey, A. (2010) A symphony of signals conduct early and late stages of adult neurogenesis. *Neuropharmacology*, **6**, 1060–1070.
24. Sanai, N., Tramontin, A.D., Quinones-Hinojosa, A., Barbaro, N.M., Gupta, N., Kunwar, S., Lawton, M.T., McDermott, M.W., Parsa, A.T., Manuel-Garcia, V.J. *et al.* (2004) Unique astrocyte ribbon in adult human brain contains neural stem cells but lacks chain migration. *Nature*, **427**, 740–744.
25. van den Berge, S.A., Middeldorp, J., Zhang, C.E., Curtis, M.A., Leonard, B.W., Mastroeni, D., Voorn, P., van de Berg, W.D., Huitinga, I. and Hol, E.M. (2010) Longterm quiescent cells in the aged human subventricular neurogenic system specifically express GFAP-delta. *Aging Cell*, **9**, 313–326.
26. Quinones-Hinojosa, A. and Chaichana, K. (2007) The human subventricular zone: a source of new cells and a potential source of brain tumors. *Exp. Neurol.*, **205**, 313–324.
27. Levison, S.W. and Goldman, J.E. (1993) Both oligodendrocytes and astrocytes develop from progenitors in the subventricular zone of postnatal rat forebrain. *Neuron*, **10**, 201–212.
28. van Strien, M.E., van den Berge, S.A. and Hol, E.M. (2011) Migrating neuroblasts in the adult human brain: a stream reduced to a trickle. *Cell Res.*, **11**, 1523–1525.
29. Shapiro, L.A., Ng, K.L., Kinyamu, R., Whitaker-Azmitia, P., Geisert, E.E., Blurton-Jones, M., Zhou, Q.Y. and Ribak, C.E. (2007) Origin, migration and fate of newly generated neurons in the adult rodent piriform cortex. *Brain Struct. Funct.*, **212**, 133–148.
30. De Marchis, S., Fasolo, A. and Puche, A.C. (2004) Subventricular zone-derived neuronal progenitors migrate into the subcortical forebrain of postnatal mice. *J. Comp. Neurol.*, **476**, 290–300.
31. Inta, D., Alfonso, J., von Engelhardt, J., Kreuzberg, M.M., Meyer, A.H., van Hooft, J.A. and Monyer, H. (2008) Neurogenesis and widespread forebrain migration of distinct GABAergic neurons from the postnatal subventricular zone. *PNAS*, **52**: 20994–20999.
32. Ridler, K., Suckling, J., Higgins, N., Bolton, P. and Bullmore, E. (2004) Standardized whole brain mapping of tubers and subependymal nodules in tuberous sclerosis complex. *J. Child Neurol.*, **19**, 658–665.
33. de Leon, G.A., Zaeri, N. and Foley, C.M. (1988) Olfactory hamartomas in tuberous sclerosis. *J. Neurol. Sci.*, **87**, 187–194.
34. Braffman, B.H., Bilaniuk, L.T., Naidich, T.P., Altman, N.R., Post, M.J., Quencer, R.M., Zimmerman, R.A. and Brody, B.A. (1992) MR imaging of tuberous sclerosis: pathogenesis of this phakomatosis, use of gadopentetate dimeglumine, and literature review. *Radiology*, **183**, 227–238.
35. Cusmai, R., Chiron, C., Curatolo, P., Dulac, O. and Tran-Dinh, S. (1990) Topographic comparative study of magnetic resonance imaging and electroencephalography in 34 children with tuberous sclerosis. *Epilepsia*, **31**, 747–755.
36. Gallagher, A., Chu-Shore, C.J., Montenegro, M.A., Major, P., Costello, D.J., Lyczkowski, D.A., Muzykewicz, D., Doherty, C. and Thiele, E.A. (2009) Associations between electroencephalographic and magnetic resonance imaging findings in tuberous sclerosis complex. *Epilepsy Res.*, **87**, 197–202.
37. Inoue, Y., Nemoto, Y., Murata, R., Tashiro, T., Shakudo, M., Kohno, K., Matsuoka, O. and Mochizuki, K. (1998) CT and MR imaging of cerebral tuberous sclerosis. *Brain Dev.*, **20**, 209–221.
38. Raznahan, A., Higgins, N.P., Griffiths, P.D., Humphrey, A., Yates, J.R. and Bolton, P.F. (2007) Biological markers of intellectual disability in tuberous sclerosis. *Psychol. Med.*, **37**, 1293–1304.
39. Bender, B.L. and Yunis, E.J. (1982) The pathology of tuberous sclerosis. *Pathol. Annu.*, **17**(Pt 1), 339–382.
40. Ess, K.C., Kamp, C.A., Tu, B.P. and Gutmann, D.H. (2005) Developmental origin of subependymal giant cell astrocytoma in tuberous sclerosis complex. *Neurology*, **64**, 1446–1449.
41. Zhou, J., Shrikhande, G., Xu, J., McKay, R.M., Burns, D.K., Johnson, J.E. and Parada, L.F. (2011) Tsc1 mutant neural stem/progenitor cells exhibit migration deficits and give rise to subependymal lesions in the lateral ventricle. *Genes Dev.*, **25**, 1595–1600.
42. Lagace, D.C., Whitman, M.C., Noonan, M.A., Ables, J.L., DeCarolis, N.A., Arguello, A.A., Donovan, M.H., Fischer, S.J., Farnbauch, L.A., Beech, R.D. *et al.* (2007) Dynamic contribution of nestin-expressing stem cells to adult neurogenesis. *J Neurosci.*, **27**, 12623–12629.
43. Shuang, M., Liu, J., Jia, M.X., Yang, J.Z., Wu, S.P., Gong, X.H., Ling, Y.S., Ruan, Y., Yang, X.L. and Zhang, D. (2004) Family-based association study between autism and glutamate receptor 6 gene in Chinese Han trios. *Am. J Med. Genet. B Neuropsychiatr. Genet.*, **131B**, 48–50.
44. Misson, J.P., Edwards, M.A., Yamamoto, M. and Caviness, V.S. Jr. (1988) Identification of radial glial cells within the developing murine central nervous system: studies based upon a new immunohistochemical marker. *Brain Res. Dev. Brain Res.*, **44**, 95–108.
45. Lacar, B., Young, S.Z., Platel, J.C. and Bordey, A. (2010) Imaging and recording subventricular zone progenitor cells in live tissue of postnatal mice. *Front Neurosci.*, **4**, 43.
46. Petreanu, L. and Alvarez-Buylla, A. (2002) Maturation and death of adult-born olfactory bulb granule neurons: role of olfaction. *J. Neurosci.*, **22**, 6106–6113.
47. Platel, J.C., Dave, K.A., Gordon, V., Lacar, B., Rubio, M.E. and Bordey, A. (2010) NMDA receptors activated by subventricular zone astrocytic glutamate are critical for neuroblast survival prior to entering a synaptic network. *Neuron*, **65**, 859–872.
48. Platel, J., Heintz, T., Young, S., Gordon, V. and Bordey, A. (2008) Tonic activation of GLUK5 kainate receptors decreases neuroblast migration in a whole mount preparation of the subventricular zone. *J. Physiol. (Lond.)*, **586**, 3783–3793.
49. Bolteus, A.J. and Bordey, A. (2004) GABA release and uptake regulate neuronal precursor migration in the postnatal subventricular zone. *J. Neurosci.*, **24**, 7623–7631.
50. Goorden, S.M., van Woerden, G.M., van der, W.L., Cheadle, J.P. and Elgersma, Y. (2007) Cognitive deficits in Tsc1+/- mice in the absence of cerebral lesions and seizures. *Ann. Neurol.*, **62**, 648–655.
51. Chan, J.A., Zhang, H., Roberts, P.S., Jozwiak, S., Wieslawa, G., Lewin-Kowalik, J., Kotulska, K. and Kwiatkowski, D.J. (2004) Pathogenesis of tuberous sclerosis subependymal giant cell astrocytomas: biallelic inactivation of TSC1 or TSC2 leads to mTOR activation. *J. Neuropathol. Exp. Neurol.*, **63**, 1236–1242.
52. Jaworski, J., Spangler, S., Seeburg, D.P., Hoogenraad, C.C. and Sheng, M. (2005) Control of dendritic arborization by the phosphoinositide-3′-kinase-Akt-mammalian target of rapamycin pathway. *J Neurosci.*, **25**, 11300–11312.
53. Kwiatkowski, D.J., Zhang, H., Bandura, J.L., Heiberger, K.M., Glogauer, M., el Hashemite, N. and Onda, H. (2002) A mouse model of TSC1 reveals sex-dependent lethality from liver hemangiomas, and up-regulation of p70S6 kinase activity in Tsc1 null cells. *Hum. Mol. Genet.*, **11**, 525–534.
54. Meikle, L., McMullen, J.R., Sherwood, M.C., Lader, A.S., Walker, V., Chan, J.A. and Kwiatkowski, D.J. (2005) A mouse model of cardiac rhabdomyoma generated by loss of Tsc1 in ventricular myocytes. *Hum. Mol. Genet.*, **14**, 429–435.
55. Platel, J.C., Gordon, V., Heintz, T. and Bordey, A. (2009) GFAP-GFP neural progenitors are antigenically homogeneous and anchored in their enclosed mosaic niche. *Glia*, **57**, 66–78.
56. Thevenaz, P., Ruttimann, U.E. and Unser, M. (1998) A pyramid approach to subpixel registration based on intensity. *IEEE Trans. Image Process*, **7**, 27–41.